Optics Letters

Coherently enhanced microwave pulses from midinfrared-driven laser plasmas

A. V. Mitrofanov,[1,2,3,4] D. A. Sidorov-Biryukov,[1,2,3] M. M. Nazarov,[3] A. A. Voronin,[1,2] M. V. Rozhko,[1,2] A. B. Fedotov,[1,2] and A. M. Zheltikov[1,2,3,5,*]

[1]Russian Quantum Center, Skolkovo, Moscow Region 143025, Russia
[2]Physics Department, International Laser Center, M.V. Lomonosov Moscow State Universityy, Moscow 119992, Russia
[3]Kurchatov Institute National Research Center, Moscow 123182, Russia
[4]Institute Laser and Information Technology–Branch of FSRC "Crystallography and Photonics," Russian Acad. Sci., Shatura, 140700, Russia
[5]Department of Physics and Astronomy, Texas A&M University, College Station, Texas 77843, USA
*Corresponding author: zheltikov@physics.msu.ru

Received 11 September 2020; revised 18 December 2020; accepted 21 December 2020; posted 21 December 2020 (Doc. ID 410030); published 24 February 2021

Ultrafast ionization of a gas medium driven by ultrashort midinfrared laser pulses provides a source of bright ultrabroadband radiation whose spectrum spans across the entire microwave band, reaching for the sub-gigahertz range. We combine multiple, mutually complementary detection techniques to provide an accurate polarization-resolved characterization of this broadband output as a function of the gas pressure. At low gas pressures, the lowest-frequency part of this output is found to exhibit a drastic enhancement as this field builds up its coherence, developing a well-resolved emission cone, dominated by a radial radiation energy flux. This behavior of the intensity, coherence, and polarization of the microwave output is shown to be consistent with Cherenkov-type radiation by ponderomotively driven plasma currents.

https://doi.org/10.1364/OL.410030

Generation of terahertz (THz) radiation by laser-induced filaments (LFs) stands out as one of the most interesting effects in ultrafast laser–plasma physics [1–3], which has been a focus of intense research within the past years, aiming at understanding the complex physics behind THz generation [4–6] and identifying laser–plasma interaction regimes whereby the highest THz yields could be achieved [6–9]. An extension of laser-filament-driven sources of low-frequency radiation below the THz borderline would help avoid strong atmospheric absorption bands, which limit long-distance transmission and remote-sensing application of THz radiation, and would help integrate cutting-edge tools of ultrafast optics and microwave photonics [10].

As significant milestones in extending laser–plasma sources to the sub-THz range, Tzortzakis *et al*. [11] have demonstrated that the spectrum of radiation emitted by LFs in air can extend down to ≈ 100 GHz, D'Amico *et al*. [12] and Brelet *et al*. [13] have reported an RF antenna emission by LFs in air, while Forestier *et al*. [14] have characterized RF conical emission from air LFs. While the generation of sub-THz radiation by LFs has been proven possible [11–18], the question as to whether this approach can enable an efficient generation of electromagnetic fields at even lower frequencies, extending to the millimeter-wave and microwave ranges, is still open. The earlier experiments [16], performed with an 800 nm Ti:sapphire laser driver, suggest that microwave radiation produced in an LF can be noticeably enhanced by lowering the gas pressure. The physics behind this effect are, however, far from trivial, as the canonical, well-established models of single-color-driven THz generation by longitudinal plasma currents (see, e.g., Refs. [4,19,20]) predict a low-frequency cutoff of broadband radiation output at around the plasma frequency, which for typical single-color laser-ionization experiments [4,16,20] ranges from 0.3 to 10 THz. The spectrum of the low-frequency output in some of these experiments, however, extends well beyond this cutoff, reaching the frequencies as low as a few gigahertz (GHz) [16].

Here, we show that ultrafast ionization of a gas medium driven by ultrashort midinfrared (mid-IR) laser pulses can provide a source of bright ultrabroadband radiation whose spectrum spans across the entire microwave band, reaching for the sub-GHz range. We combine multiple mutually complementary detection techniques to provide an accurate polarization-resolved characterization of this broadband output as a function of the gas pressure p. At low p, the lowest-frequency part of this output is shown to exhibit a drastic enhancement, as this field builds up its coherence, developing a well-resolved emission cone, dominated by a radial radiation energy flux.

Central to our approach to the enhancement of microwave generation is the idea of designing a suitable laser–plasma interaction setting in which the mid-IR-laser-driven ponderomotive force would induce adequately long-lived plasma currents, as needed for the extension of output spectra toward lower frequencies. Providing a guide for this search are the equations for the secondary radiation field outside the laser plasma as derived by Sprangle *et al*. [19], with a ponderomotive source term $\tilde{\psi}_p(r, k, \omega) \approx (4\pi/c^2)(1 + i\nu_e/\omega)^{-1}\tilde{S}(r, k, \omega)$, where r is the radial coordinate, ω is the radiation frequency,

ν_e is the collision rate, k is the pertinent wave-vector component, c is the speed of light in vacuum, $\tilde{S}(r, k, \omega) = \iint_{-\infty}^{\infty} S(r, z, t)\exp(-kz + i\omega t)\mathrm{d}z\mathrm{d}t$, $S(r, z, t) \approx -e^3(2m\omega_0)^{-2} \rho(r, z, t)\partial|E_L(r, z, t)|^2/\partial z$, $E_L(r, z, t)$ is the electric field of the driver pulse, z is the coordinate in the direction of pulse propagation, ω_0 is the driver frequency, and ρ, e, and m are the electron density, electron charge, and electron mass, respectively. This model has been shown to explain many of the important properties of THz radiation in single-color laser-filamentation experiments [4,20,21].

The spectrum of the ponderomotive source term displays a low-frequency cutoff at $\omega \approx \nu_e$. To understand the behavior of $|\tilde{\psi}_p(r, k, \omega)|$ as a function of the gas pressure p around this cutoff, we group the pressure-dependent factors in $|\tilde{\psi}_p(r, k, \omega)|$ as $R(p) = \rho I_0/(\nu_e \tau_L)$, with I_0 and τ_L being typical values of peak field intensity and pulse width in the laser driver. All the factors in $R(p)$ should be found through a self-consistent solution of suitable coupled equations for the spatiotemporal evolution of the driver and dynamics of laser-induced ionization. In our model, a standard (2 + 1)-dimensional nonlinear evolution equation for an ultrashort laser pulse [22,23] is solved jointly with the equation for the electron density, $d\rho(t)/dt = w(t)[\rho_0 - \rho(t)]$, where w is the ionization rate, and ρ_0 is the density of neutral species undergoing ionization by the laser driver. With atmospheric air at a variable pressure p chosen as a gas target, we calculate $w(t)$ using the Keldysh-model-based approach with the ionization potential U_0 set equal to the U_0 of molecular oxygen, $U_0 = 12.1$ eV. The collision rate is calculated as [24] $\nu_e = \nu_{eO} + \nu_{eN} + \nu_{ei}$, where ν_{eO} and ν_{eN} are the rates of electron collisions with, respectively, O_2 and N_2 molecules in air, and ν_{ei} is the rate of electron–ion collisions. Numerical simulations were performed using shared supercomputation facilities at M.V. Lomonosov Moscow State University.

In Figs. 1(a) and 1(b), we present the results of numerical modeling performed for a laser pulse with a central wavelength of $\lambda_0 = 3.9$ µm, pulse width of $\tau_0 \approx 80$ fs, and pulse energy of $E_0 \approx 7$ mJ focused in air using a mirror or a lens with a focal length of $f = 50$ cm. As one of the general tendencies of this coupled driver-plasma dynamics, the laser field gives rise to a rapid buildup of the electron density $\rho(r, z, t)$ [Fig. 1(b)], as its intensity increases toward the beam waist [Fig. 1(a)], inducing a transverse profile of the refractive index $\delta n_p(r, z, t) \approx -[\omega_p(r, z, t)]^2/(2\omega_0^2)$, with $\omega_p(r, z, t) = [4\pi e^2 \rho(r, z, t)/m]^{1/2}$ being the plasma frequency. Such a profile of δn_p leads to a refraction of the laser beam, modifying the beam-focusing geometry compared to beam focusing in the absence of plasmas [shown by the dashed line in Fig. 1(a)], arresting a further growth of the field intensity $|E_L(r, z, t)|^2$ along z [Fig. 1(b)] and limiting, via lower ionization rates, the electron density at a level of $\rho \approx 2.3 \cdot 10^{17}$ cm^{-3} [Fig. 1(b)]. The collision rate is dominated by electron–molecule collisions and is estimated in this regime as $\nu_e \approx 3.5$ THz.

While these tendencies are observed within a broad range of gas pressures, plasma refraction and related field-intensity-limiting effects are much weaker at lower p. Specifically, for $p = 0.1$ bar, ionization-induced beam refraction remains insignificant until much later in beam dynamics, i.e., until much higher field intensities are achieved in a focused beam at larger z [the solid line in Fig. 1(a)]. The maximum field intensity in

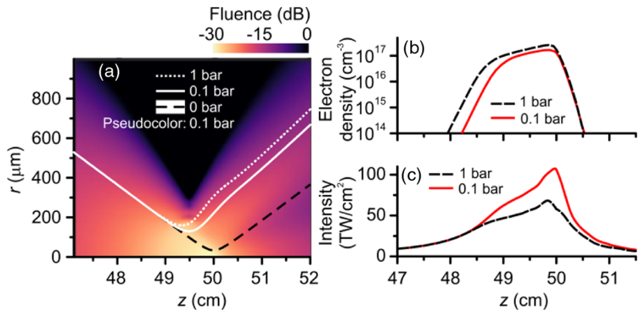

Fig. 1. Numerical modeling for air plasma induced by a laser pulse with $\lambda_0 = 3.9$ µm, $\tau_0 \approx 80$ fs, and $E_0 \approx 7$ mJ focused with $f = 50$ cm. (a) Laser field intensity integrated over the pulse $F(r, z) = \int_{-\infty}^{\infty} I(r, t, z)\mathrm{d}t$ as a function of r and z for $p = 0.1$ bar. Also shown is the beam radius, $r_L(z) = [\int_0^{\infty} F(r, z)2\pi r^3 \mathrm{d}r]/[\int_0^{\infty} F(r, z)2\pi r \mathrm{d}r]$, for $p = 0$ (dashed line), 0.1 bar (solid line), and 1 bar (dotted line). (b) The on-axis electron density and (c) field-intensity profiles along the propagation coordinate z for $p = 0.1$ bar (solid lines) and 1 bar (dashed lines).

this regime, $I_0 \approx 100$ TW/cm^2, is a factor of $\approx$1.7 higher than typical I_0 values attainable at $p = 1$ bar [cf. solid and dashed red lines in Fig. 1(b)]. Because the driver intensity reaches much higher values at lower p, a decrease in the electron density is not as large as one would expect based only on lower ρ_0, decreasing linearly with p. Indeed, while the pressure has dropped by a factor of 10 relative to the case of $p = 1$ bar, a typical electron density, $\rho \approx 1.7 \cdot 10^{17}$ cm^{-3}, has only decreased by a factor of $\approx$ 1.5 [solid and dashed lines in Fig. 1(b)]. With the collision rate estimated at $\nu_e \approx 0.35$ THz in this regime, an increase in $R(p)$ is more than an order of magnitude.

As an important factor enhancing microwave generation, the collision rate ν_e in mid-IR-driven air plasmas is dominated by electron-neutral collisions within a broad range of gas pressures, extending to p as low as a few millibars, effectively decoupling $\nu_e(p)$ from $\rho(p)$ for enhanced microwave generation. Thus, not only does longer λ_0 increase the ponderomotive source term $\tilde{\psi}_p(r, k, \omega)$ via the $1/\omega_0^2$ factor in $S(r, z, t)$, but it also provides a comfortable gap between the electron-neutral and electron–ion collision rates, with ν_{eO}, $\nu_{eN} \propto W_e^{1/2}$, $\nu_{ei} \propto W_e^{-3/2}$, and W_e being the electron kinetic energy, increasing their ratio as, roughly, $\nu_{eO,eN}/\nu_{ei} \propto W_e^2 \propto \lambda_0^4$.

Driver pulses are delivered in our experiments (Fig. 2) by a pulse-compressed output of a three-stage optical parametric chirped-pulse amplifier (OPCPA) [25]. The OPCPA is set to deliver mid-IR pulses with a central wavelength of $\lambda_0 \approx 3.9$ µm and a pulse width of $\tau_0 \approx 80$ fs. While pulse energies up to $E_0 \approx$ 35 mJ are available at the output of this OPCPA, pulses with E_0 below $\approx 10 - 15$ mJ were found to be best suited for the purpose of our studies, providing a broadband output (Figs. 3 and 4) with a spectrum spanning across the entire microwave range [Fig. 3(b)].

The mid-IR OPCPA output is focused into a gas cell with a lens (Fig. 2) with a focal length of 50 cm. The gas pressure p inside the cell is varied from 0.1 mbar up to 1.0 bar. For two-color laser–plasma experiments, a 0.5-mm-thick $AgGaS_2$ crystal (AGS in Fig. 2), placed right behind the CaF_2 gas-cell entrance window, is used for second-harmonic (SH) generation. The focused single-color (the 3.9 µm only OPCPA output) or two-color (the 3.9 µm field and its SH) field drives a gas target,

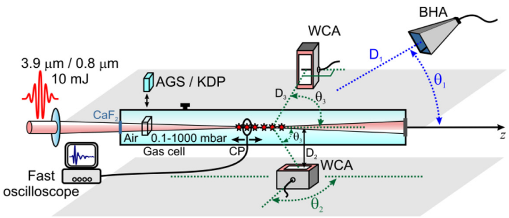

Fig. 2. Microwave radiation generation in microplasmas driven by ultrashort mid-IR pulses: WCA, waveguide-to-coaxial adapter; BHA, broadband horn antenna; CP, Rogowski-coil-type current probe.

giving rise to broadband radiation, which exits the gas cell to be subjected to a spectral and temporal analysis (Fig. 2).

Microwave radiation is detected in our experiments (Fig. 2) using a waveguide-to-coaxial adapter (WCA), covering a detection range from 8 to 12 GHz, and a broadband horn antenna (BHA), whose detection sensitivity is well-calibrated at least within the range from 0.5 to 20 GHz and that provides a reasonable, albeit less accurately calibrated, detection sensitivity all the way down to 0.1 GHz. Microwave waveform characterization is augmented by z-resolved microwave waveform measurements, performed with the use of a copper-wire B-dot current probe (CP) [3,17], placed on a z-scanned translation stage (Fig. 2). The signals detected by the WCA, BHA, and CP are analyzed and recorded with a 50 GHz Tektronix oscilloscope. Polarization of microwave radiation is analyzed by rotating the WCA about the normal to its aperture and detecting the microwave output as a function of the angle θ_2 between the WCA coaxial probe and the z axis (Fig. 2). Microwave radiation patterns are studied by scanning the WCA detector in the angle θ_3 between the z axis and the line connecting the plasma source and the WCA (Fig. 2).

In Fig. 3(a), we present a typical BHA trace of the microwave field induced by a single-color laser driver with $\lambda_0 \approx 3.9$ μm, $E_0 \approx 10$ mJ, and $\tau_0 \approx 80$ fs in a gas cell filled with atmospheric air at $p \approx 60$ mbar. The BHA in this experiment is placed at a distance of $D_1 \approx 0.8 - 1.5$ m from the laser–plasma source at an angle of $\theta_1 \approx 47^\circ$ relative to the driver propagation axis (Fig. 2). Spectral analysis of microwave traces from low-pressure laser plasmas performed via wavelet transform with multilevel soft thresholding reveals a reliably detectable spectral content extending all the way down to the sub-GHz range (Fig. 4).

As one of the central results of our study, the microwave output of laser-induced plasmas is found to be critically sensitive to the gas pressure [Fig. 3(c)]. With the pulse energy of a single-color 3.9 μm, 80 fs laser driver set at $E_0 \approx 10$ mJ and with the gas pressure kept below $p \approx 20$ mbar, the BHA readout is seen to continue growing toward lower p. This behavior is in striking contrast with the pressure dependence of the WCA signal, which reaches its maximum at around $p \approx 20$ mbar, falling off toward lower p. This result indicates the enhancement of the lowest-ω part of the output spectrum. Indeed, since the WCA is blind to radiation with $\omega/2\pi < \nu_{\mathrm{WCA}} \approx 8$ GHz, while the BHA detection range extends well beyond ν_{WCA}, enhancement of microwave radiation with $\omega/2\pi < 8$ GHz has to show up as a difference in the BHA and WCA readouts at low gas pressures, exactly as observed in experiments. This finding is fully consistent with the BHA measurements (Fig. 4), which confirm a significant enhancement in the lowest-ω part of the output spectrum at low gas pressures. Indeed, as the gas pressure is lowered in these experiments from 100 to 1 mbar, the

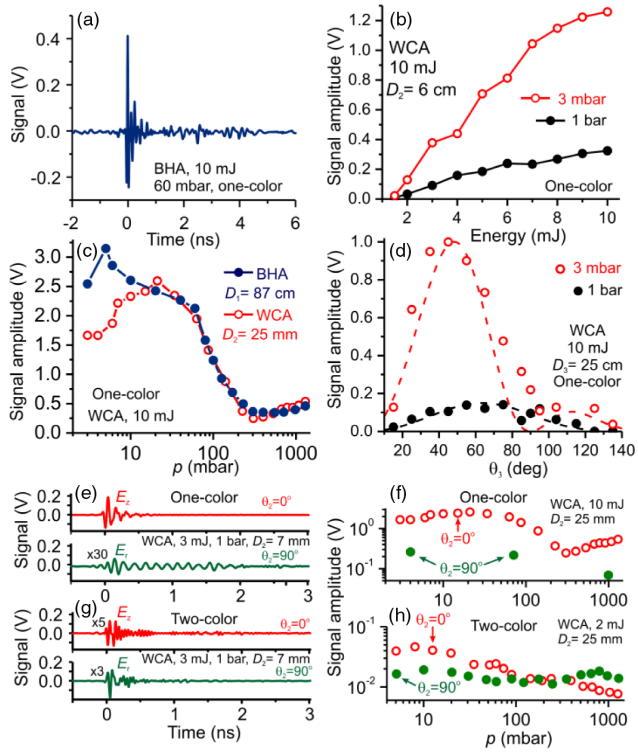

Fig. 3. (a) BHA trace of the microwave field induced by a laser driver with $\lambda_0 \approx 3.9$ μm, $E_0 \approx 10$ mJ, and $\tau_0 \approx 80$ fs in a gas cell filled with atmospheric air at $p \approx 60$ mbar measured with $D_1 \approx 1.5$ m and $\theta_1 \approx 47^\circ$. (b) Microwave signal as a function of the driver pulse energy measured with the WCA at $D_2 \approx 60$ mm, $\theta_2 \approx 0^\circ$, and $\theta_3 \approx 47^\circ$ with $\lambda_0 \approx 3.9$ μm and $\tau_0 \approx 80$ fs at $p \approx 3$ mbar (open circles, red curve) and 1 bar (filled circles, black curve). (c) Microwave signal as a function of p measured with the WCA at $D_2 \approx 25$ mm, $\theta_3 \approx 50^\circ$ (open circles, red curve) and the BHA at $D_1 \approx 87$ cm and $\theta_1 \approx 47^\circ$ (filled circles, blue curve) for $\lambda_0 \approx 3.9$ μm, $E_0 \approx 10$ mJ, and $\tau_0 \approx 80$ fs. (d) Microwave signal as a function of θ_3 with the WCA at $D_3 \approx 25$ cm for $p \approx 3$ mbar (open circles, red curve) and 1000 mbar (filled circles, black curve), $\lambda_0 \approx 3.9$ μm, $E_0 \approx 10$ mJ, $\tau_0 \approx 80$ fs: (circles) experimental results, (dashed line) their best $\Phi(\theta_3)$ fit. (e), (g) Polarization-resolved time traces and (f), (h) pressure scans of the microwave output measured with the WCA at $\theta_3 \approx 47^\circ$ and $\theta_2 \approx 0^\circ$ (open circles, red lines) and $\theta_2 \approx 90^\circ$ (filled circles, green line): experiments with (e), (f) a $\lambda_0 \approx 3.9$ μm, $\tau_0 \approx 80$ fs single-color driver with (e) $E_0 \approx 3$ mJ, $D_2 \approx 7$ mm, $p \approx 1$ bar and (f) $E_0 \approx 10$ mJ, $D_2 \approx 25$ mm and (g), (h) two-color driver consisting of the 3.9 μm, 80 fs field and its $\pi/2$-phase-shifted SH with $E_{\mathrm{SH}} \approx 0.1$ mJ, $\tau_{\mathrm{SH}} \approx 70$ fs.

intensity of the $\omega/2\pi < 8$ GHz part of the microwave output increases by more than an order of magnitude (Fig. 4), in strong correlation with a pressure behavior of the low-frequency cutoff in the spectrum of $|\tilde{\psi}_p(r, k, \omega)|$.

The low-pressure enhancement of microwave radiation also strongly correlates with the low-p pressure behavior of its radiation pattern, which, in its turn, displays a profound change in response to a decrease in the gas pressure. Shown in Fig. 3(d) is a typical behavior of the microwave signal P_{m} as a function of θ_3, measured by scanning the WCA (Fig. 2) with the distance D_3 between the CWA and the plasma source fixed at $D_3 \approx 25$ cm. At high gas pressures [$p = 1$ atm in Fig. 3(d)], the angular dependence of P_{m} is seen to be very weak, if resolvable at all. At low gas pressures, however, the behavior of $P_{\mathrm{m}}(\theta_3)$ is strikingly

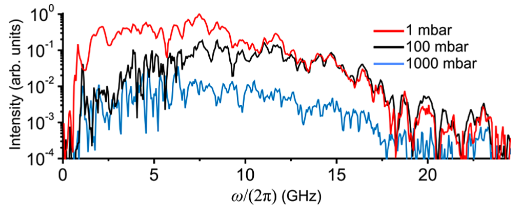

Fig. 4. BHA spectra of microwave radiation induced by a laser driver with $\lambda_0 \approx 3.9$ μm, $E_0 \approx 10$ mJ, and $\tau_0 \approx 80$ fs in a gas cell filled with atmospheric air at pressure p, as shown in the plots. The BHA detector is placed at $\theta_1 \approx 47^\circ$, $D_1 \approx 1.5$ m from the plasma source.

different. At $p \approx 3$ mbar [red line in Fig. 3(d)], $P_\mathrm{m}(\theta_3)$ is seen to display a well-resolved peak at $\theta_3 \approx 45^\circ$, indicating a buildup of spatial coherence in the sub-THz microwave field.

In Fig. 3(d), this behavior of $P_\mathrm{m}(\theta_3)$ is compared with a fringe structure of Cherenkov-type conical radiation emitted by longitudinal plasma currents [5,20], $\Phi(\theta_3) = \sin^2\theta_3 \sin^2[(\omega_0/c) L \sin^2(\theta_3/2)]/\sin^4(\theta_3/2)$, with L being the plasma channel length. With $\omega_0 \approx 10$ GHz, as dictated by the spectrum of this signal, the best fit for $p = 3$ and 1000 mbar is achieved [cf. the circles and dashed lines in Fig. 3(d)] with $L \approx 1.6$ and 3 cm, respectively. That the plasma channel length L increases with growing p is seen from both z-resolved CP plasma scans and simulations in Fig. 1. Moreover, the best-fit L values in Fig. 3(d) agree well with the beam-waist lengths found from modeling in Fig. 1. The first-lobe maximum of $\Phi(\theta_3)$ is achieved at $\theta_\mathrm{m} \approx 47^\circ$ for $p \approx 3$ mbar [red curve in Fig. 3(d)] and $\theta_\mathrm{m} \approx 70^\circ$ for $p \approx 1$ bar [black curve in Fig. 3(d)], in close agreement with angle-resolved measurements [red and black circles in Fig. 3(d)].

In Figs. 3(e) and 3(f), we present polarization-resolved time traces and pressure scans of the microwave output measured with the WCA detector placed in the near field to probe the evanescent field of the microwave output. The z-polarized component of the microwave field, E_z, detected at $p \approx 1$ bar with the WCA oriented at $\theta_2 \approx 0^\circ$ [red line in Figs. 3(e) and 3(f)] is seen to be an order of magnitude stronger than its orthogonal counterpart, E_r, probed with the WCA oriented at $\theta_2 \approx 90^\circ$ [green line in Figs. 3(e) and 3(f); note a magnifying factor of 30 in Fig. 3(e)]. This polarization structure of the microwave output is indicative of the dominant role of ponderomotively driven longitudinal wakefields [4,6,19–21,26] as a source of microwave radiation. That the E_r component is not vanishing, on the other hand, suggests that the ponderomotive wakefields inside the plasma are not purely longitudinal. The E_r component, however, does not make it to the far field. When the WCA is placed at $D_2 > 40$ cm, its readout is maximum at $\theta_2 = 0^\circ$ and vanishes at $\theta_2 = 90^\circ$, exactly as expected for radiation generated by purely longitudinal wakefields [4,19,20].

Microwave radiation with drastically different polarization properties is observed in experiments with a two-color driver [Figs. 3(g) and 3(h)]. In these experiments, the 3.9 μm, 80 fs OPCPA output is mixed with its $\pi/2$-phase-shifted SH to yield a field with broken time symmetry [3]. Such a two-color field induces transverse photoionization currents that do not cancel within the field cycle, giving rise to a detectable E_r mode in THz-microwave radiation [3,18,27]. Transverse currents often dominate the generation of THz radiation in LF experiments [3,27]. Polarization- and pressure-resolved analysis performed in our study suggests that, for lower ω, i.e., for the microwave component of plasma radiation [Figs. 3(g) and 3(h)], both the transverse and longitudinal currents can play an important role, with their relative significance changing with p [Fig. 3(h)].

Funding. Welch Foundation (A-1801-20180324); Russian Science Foundation (18-72-10109 – mid-IR photonics, 20-12-00088 – ultrabroadband nonlinear optics); Russian Foundation for Basic Research (18-02-40034, 18-29-20031, 18-32-20196, 18-02-40031, 20-21-00140, 19-02-00473).

Disclosures. The authors declare no conflicts of interest.

REFERENCES

1. D. J. Cook and R. M. Hochstrasser, Opt. Lett. **25**, 1210 (2000).
2. X. Xie, J. Dai, and X.-C. Zhang, Phys. Rev. Lett. **96**, 075005 (2006).
3. K. Y. Kim, A. J. Taylor, J. H. Glownia, and G. Rodriguez, Nat. Photonics **2**, 605 (2008).
4. C. D'Amico, A. Houard, M. Franco, B. Prade, A. Mysyrowicz, A. Couairon, and V. T. Tikhonchuk, Phys. Rev. Lett. **98**, 235002 (2007).
5. N. Karpowicz and X.-C. Zhang, Phys. Rev. Lett. **102**, 093001 (2009).
6. Y. S. You, T. I. Oh, and K. Y. Kim, Phys. Rev. Lett. **109**, 183902 (2012).
7. M. Clerici, M. Peccianti, B. E. Schmidt, L. Caspani, M. Shalaby, M. Giguère, A. Lotti, A. Couairon, F. Légaré, T. Ozaki, D. Faccio, and R. Morandotti, Phys. Rev. Lett. **110**, 253901 (2013).
8. D. Jang, R. M. Schwartz, D. Woodbury, J. Griff-McMahon, A. H. Younis, H. M. Milchberg, and K.-Y. Kim, Optica **6**, 1338 (2019).
9. Z. Zhang, Y. Chen, S. Cui, F. He, M. Chen, Z. Zhang, J. Yu, L. Chen, Z. Sheng, and J. Zhang, Nat. Photonics **12**, 554 (2018).
10. J. Capmany and D. Novak, Nat. Photonics **1**, 319 (2007).
11. S. Tzortzakis, G. Méchain, G. Patalano, Y.-B. André, B. Prade, M. Franco, A. Mysyrowicz, J.-M. Munier, M. Gheudin, G. Beaudin, and P. Encrenaz, Opt. Lett. **27**, 1944 (2002).
12. C. D'Amico, A. Houard, M. Pellet, Ch. Pichot, and A. Mysyrowicz, J. Phys. D **41**, 245206 (2008).
13. Y. Brelet, A. Houard, G. Point, B. Prade, J. Carbonnel, Y.-B. Andre, M. Pellet, and A. Mysyrowicz, Appl. Phys. Lett. **101**, 264106 (2012).
14. B. Forestier, A. Houard, M. Durand, Y.-B. André, B. Prade, J.-Y. Dauvignac, F. Perret, C. Pichot, M. Pellet, and A. Mysyrowicz, Appl. Phys. Lett. **96**, 141111 (2010).
15. F. Théberge, J.-F. Gravel, J.-C. Kieffer, F. Vidal, and M. Châteauneuf, Appl. Phys. Lett. **111**, 073501 (2017).
16. A. Englesbe, J. Elle, R. Reid, A. Lucero, H. Pohle, M. Domonkos, K. Krushelnick, and A. Schmitt-Sody, Opt. Lett. **43**, 4953 (2018).
17. T. I. Oh, Y. S. You, N. Jhajj, E. W. Rosenthal, H. M. Milchberg, and K. Y. Kim, New J. Phys. **15**, 075002 (2013).
18. A. V. Mitrofanov, D. A. Sidorov-Biryukov, M. M. Nazarov, A. A. Voronin, M. V. Rozhko, A. D. Shutov, S. V. Ryabchuk, E. E. Serebryannikov, A. B. Fedotov, and A. M. Zheltikov, Optica **7**, 15 (2020).
19. P. Sprangle, J. Peñano, B. Hafizi, and C. Kapetanakos, Phys. Rev. E **69**, 066415 (2004).
20. C. D'Amico, A. Houard, S. Akturk, Y. Liu, M. Franco, B. Prade, A. Couairon, V. Tikhonchuk, and A. Mysyrowicz, New J. Phys. **10**, 013015 (2007).
21. C. D'Amico, A. Houard, M. Franco, B. Prade, and A. Mysyrowicz, Opt. Express **15**, 15274 (2007).
22. A. Couairon and A. Mysyrowicz, Phys. Rep. **441**, 47 (2007).
23. L. Bergé, S. Skupin, R. Nuter, J. Kasparian, and J.-P. Wolf, Rep. Prog. Phys. **70**, 1633 (2007).
24. Yu. P. Raizer, *Gas Discharge Physics* (Springer, 1991).
25. A. V. Mitrofanov, A. A. Voronin, D. A. Sidorov-Biryukov, A. Pugžlys, E. A. Stepanov, G. Andriukaitis, T. Flöry, S. Ališauskas, A. B. Fedotov, A. Baltuška, and A. M. Zheltikov, Sci. Rep. **5**, 8368 (2015).
26. I. Thiele, R. Nuter, B. Bousquet, V. Tikhonchuk, S. Skupin, X. Davoine, L. Gremillet, and L. Bergé, Phys. Rev. E **94**, 063202 (2016).
27. A. D. Koulouklidis, C. Gollner, V. Shumakova, V. Yu. Fedorov, A. Pugžlys, A. Baltuška, and S. Tzortzakis, Nat. Commun. **11**, 292 (2020).